THREE-DIMENSIONAL LONGWAVE INFRARED (LWIR) SYNTHETIC IMAGE GENERATION INCORPORATING ANGULAR EMISSIVITY EFFECTS USING RAY-TRACING TECHNIQUES

Eric H. Shor, Carl Salvaggio, and John R. Schott

Rochester Institute of Technology
Center for Imaging Science
Digital Imaging and Remote Sensing Laboratory
One Lomb Memorial Drive
Rochester, New York 14623-0887

ABSTRACT

A technique for longwave infrared (LWIR) synthetic image generation (SIG) is shown which yields improved radiometric accuracy in the 8-14 μm bandpass. This process uses a modified LOWTRAN 6 atmospheric transmission/upwelled radiance code and computer graphics ray-tracing techniques. A scene is created by placing faceted objects into world coordinates with rotation, translation, and scaling parameters. Each facet is assigned a material index and temperature. The material index points to optical properties for that material. The modified LOWTRAN 6 code incorporates sensor response function when computing tables of the atmospheric transmission and upwelled and downwelled radiances. A ray-traced image is then generated. A final synthetic LWIR scene is generated to geometrically match an actual acquired scene so that radiometric comparisons can be made.

INTRODUCTION

The last 25 years have seen the need develop for artificially created images in such fields as animation, computer-aided design and manufacturing (CAD/CAM), and flight simulation. Most of these applications have been associated with the computer graphics community. The algorithms for creating such imagery are collectively known as synthetic image/scene generation. The majority of these techniques, however, have been applied in the visible part of the electromagnetic spectrum. LWIR SIG presents many unique problems not seen in conventional applications since the target's kinetic temperature dominates the signal received by the sensor.

One application of LWIR SIG is to provide input to Automatic Target Recognition (ATR) routines. These routines require a sequence of images to evaluate tracking algorithms. The evaluation of sensor performance before actual prototyping is also of interest. Other applications include training, mission planning, and background clutter characterization. Salvaggio and Schott (1989) presented a model that accurately predicted LWIR phenomena using 2-D image templates. It is the goal of this effort to incorporate this radiometric model into a versatile 3-D simulator.

Creation of a credible computer generated image requires realistic 3-D modeling. Realistic appearance of objects in the scene is based largely on material properties and lighting conditions. Simulation of proper illumination conditions is a critical and complex task. The technique of ray-tracing, borrowed from the computer graphics community, has been developed to simulate illumination. The direction of propagation of radiant flux from the source to the scene is called the path. Along this path, the flux can be absorbed, transmitted, scattered or reflected by either the target, its background or the atmosphere. It is most important to realize that every object within the scene above 0° K is a source, thus establishing the difference from conventional ray tracing techniques. Since the atmosphere is important as a source (as well as an attenuator) we therefore need to include atmospheric propagation for realistic scene simulation. Atmospheric models such as LOWTRAN [Kneizys *et al.* (1983)] and FASCOD2 [Clough *et al.* (1986)] can been used to mimic the effects of the atmosphere.

The radiance from an object in the infrared is due primarily to its temperature and its material characteristics. The thermal environment of an object has a major impact on its IR radiance. The environment may cause a change in the object's temperature and thus alter its thermal signature. For example, object temperature may rise due to exposure to sunlight or proximity to other hot objects (such as internal heat sources like an engine). Additional environmental variables that affect object temperature include wind speed and cloud cover.

Previous work in LWIR SIG [Sheffer and Cathcart (1988)] and [Stets *et al.* (1988)] have created very detailed and complex computer simulation codes. This study will address a small portion of the process in an attempt to improve the radiometry and atmospheric propagation effects. Diurnal cycles, background clutter, texture, heat flux, and terrain elevation data are not included in the treatment presented here.

TECHNICAL APPROACH

The effective radiance reaching a sensing platform in the 8-14 μm region at an altitude h and view angle θ can be expressed as

$$L(h,\theta) = \varepsilon(\theta)\, L_T\, \tau + [1-F]\, r\,(\theta)\, L_b \tau + F\, r(\theta)\, L_d\, \tau + L_u(h,\theta) \qquad (1)$$

where $\varepsilon(\theta)$ is the angular hemispheric emissivity, $r(\theta)$ is the angular hemispheric reflectance, L_T is the radiance from a blackbody at temperature T, L_d is the downwelled radiance from the hemisphere above the target, L_b is the background radiance upon the target, $\tau(h,\theta)$ is the atmospheric transmission to altitude h through view angle θ, $L_u(h,\theta)$ is the upwelled radiance reaching a sensor caused by self-emission and scattering in the intervening air column, and F is the fraction of the hemisphere above the target which is sky. Note that spectral dependency of each of these terms has been omitted and it is assumed we are dealing with integrated estimates.

In many cases the diffuse downwelled radiance incident on a reflecting surface is not from the sky alone. In the case of varying topography, the element being observed may also be irradiated from adjacent terrain elements. In this case, we observe that the downwelled radiance, L_d, may be composed of radiance from neighboring surfaces, L_b.

The characterization of material properties has always been a difficult task. Ideally, bidirectional reflectance distribution functions (BRDF) for each material should be used. However, in order to simplify the model, materials have been classified into two categories, specular and diffuse. Specular reflectors are assumed ideal so the angle of incidence equals the angle of reflection. Diffuse reflectors are assumed lambertian, *i.e.* reflecting equal radiance into all directions.

For a specular reflector, it is known that the background objects' radiance is very important. The question arises as to how many times energy can "bounce" and still remain significant? Figure 1 presents a scenario where the target is the ground, the house is the ground's background, and the tree is the house's background. When viewing the ground, is the tree's radiance a significant portion of the total signal? It was shown by Shor (1990) that for temperatures near Earth ambient, only a single bounce need be considered significant. The effective temperature when two backgrounds were taken into account was not significantly different from the inclusion of just one.

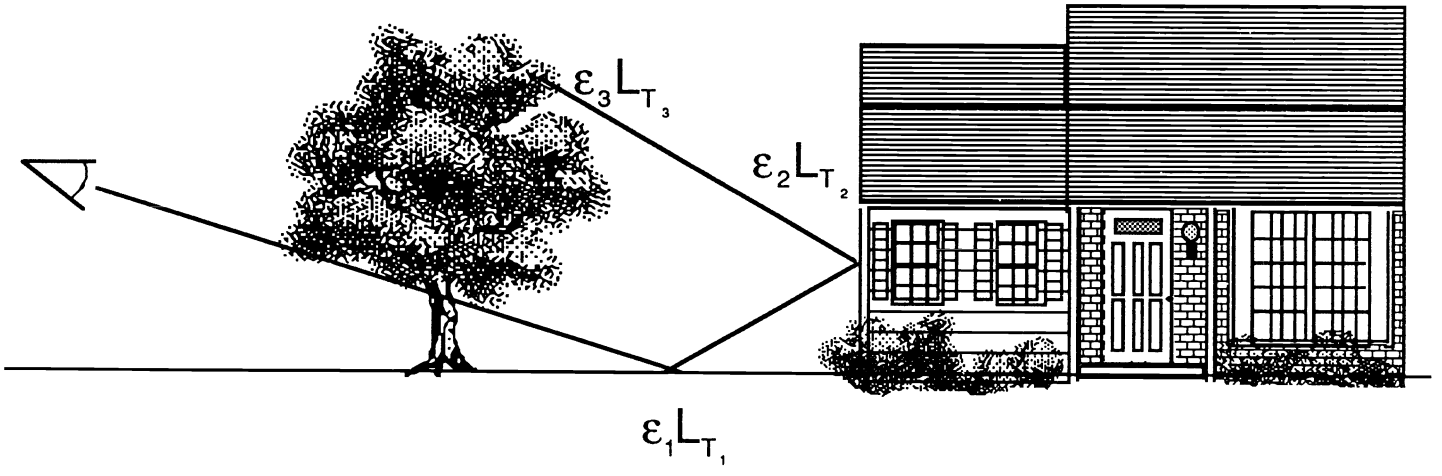

FIGURE 1 Illustration of multiple bounces for radiation propagation

The shape factor, F, is another parameter that needs to be addressed. This parameter is very difficult to calculate because it is dependent on adjacent scene elements. Figure 2 illustrates the geometry of this parameter. An object may only see a fraction of the sky in some cases while in others it can see the entire hemisphere above it. If the background in Figure 2 were not there, the value of the downwelled radiance (L_d) would simply be the integral over the hemispheric skydome. In order to incorporate the shape factor, the term F needs to be calculated for each pixel. This could be done by sending out a series of rays

from each point and counting the number of intersections with non-sky background. This would be a time consuming task so the value of F was ignored in this initial study. For lambertian or near lambertian objects with shape factor F of approximately 0.75 and background near ambient the error in assuming F to be unity is of the order of 1.0°K.

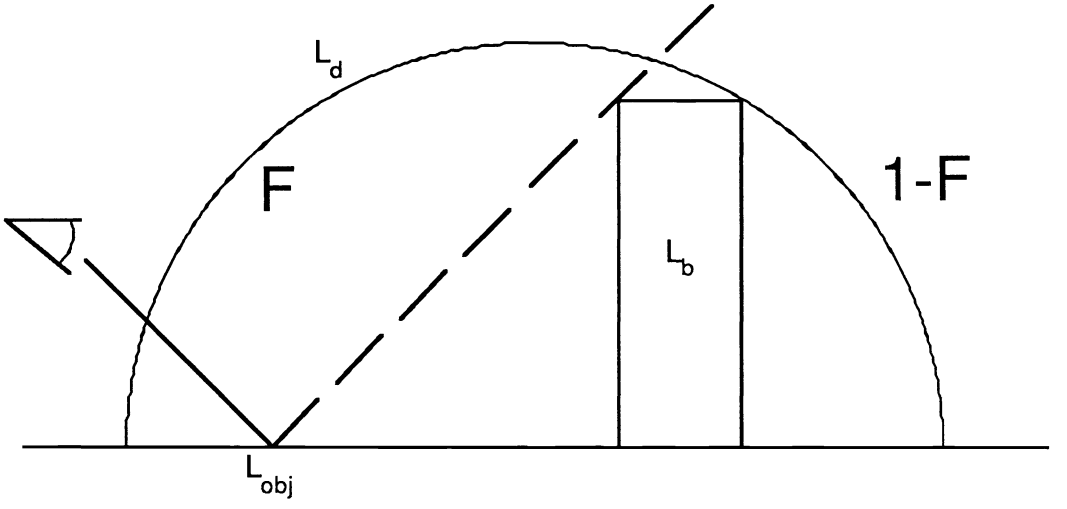

$$L = \varepsilon L_{obj} + (1-\varepsilon)[FL_d + (1-F)L_b]$$

FIGURE 2 Illustration of the concept of the shape factor (F)

Atmospheric conditions in the form of radiosonde data are input to the modified LOWTRAN 6 atmospheric transmission/upwelled radiance model [Kneizys (1983)]. The transmission along with the upwelled and downwelled radiance values are calculated and incorporated into the radiometric determinations.

EXPERIMENTAL APPROACH

Before energy is propagated through the atmosphere to a sensor, we need to calculate the radiance leaving the target at the ground (h=0) in the direction of the sensor, $L(0,\theta)$. τ and L_u need not be considered at this time as they can be incorporated later. Equation 1 reduces to

$$L(0,\theta) = \varepsilon(\theta)\, L_T + r(\theta)\, [\, L_d(\theta) + L_b(\theta)\,] \qquad (2)$$

where $\varepsilon(\theta)$ is obtained from experimental data [Schott (1986)] and stored in a look-up-table (LUT). Since most objects have low transmittance in the infrared, Kirchhoff's law states that a unit sum exists for reflectivity and emissivity yielding $r(\theta) = 1 - \varepsilon(\theta)$. L_T has been pre-calculated and stored in a LUT for a series of likely encountered temperatures, speeding up execution of the SIG since Planck's equation need not be evaluated for every

temperature encountered. Ray-tracing techniques are used to determine L_d and L_b for each pixel. It is assumed that all materials fall into two categories, specular or diffuse reflectors. A specular object will act as a perfect reflector (no BRDF assumed) and the downwelled radiance will be due either to the sky (L_d) or the background (L_b).

Solution of Equation 2 starts with projection of a primary ray backwards from the sensor representing the flux path. If it hits a diffuse object, the integrated downwelled radiance L_d is calculated. If the object is specular, a secondary ray (reflection) is projected. If that secondary ray hits an object, then $L_b = L_{T_b}$ for that background object. However, if the secondary ray does not hit an object, the angular downwelled radiance $L_d(\theta)$ will be calculated and incorporated as L_b (*c.f.* Figure 3).

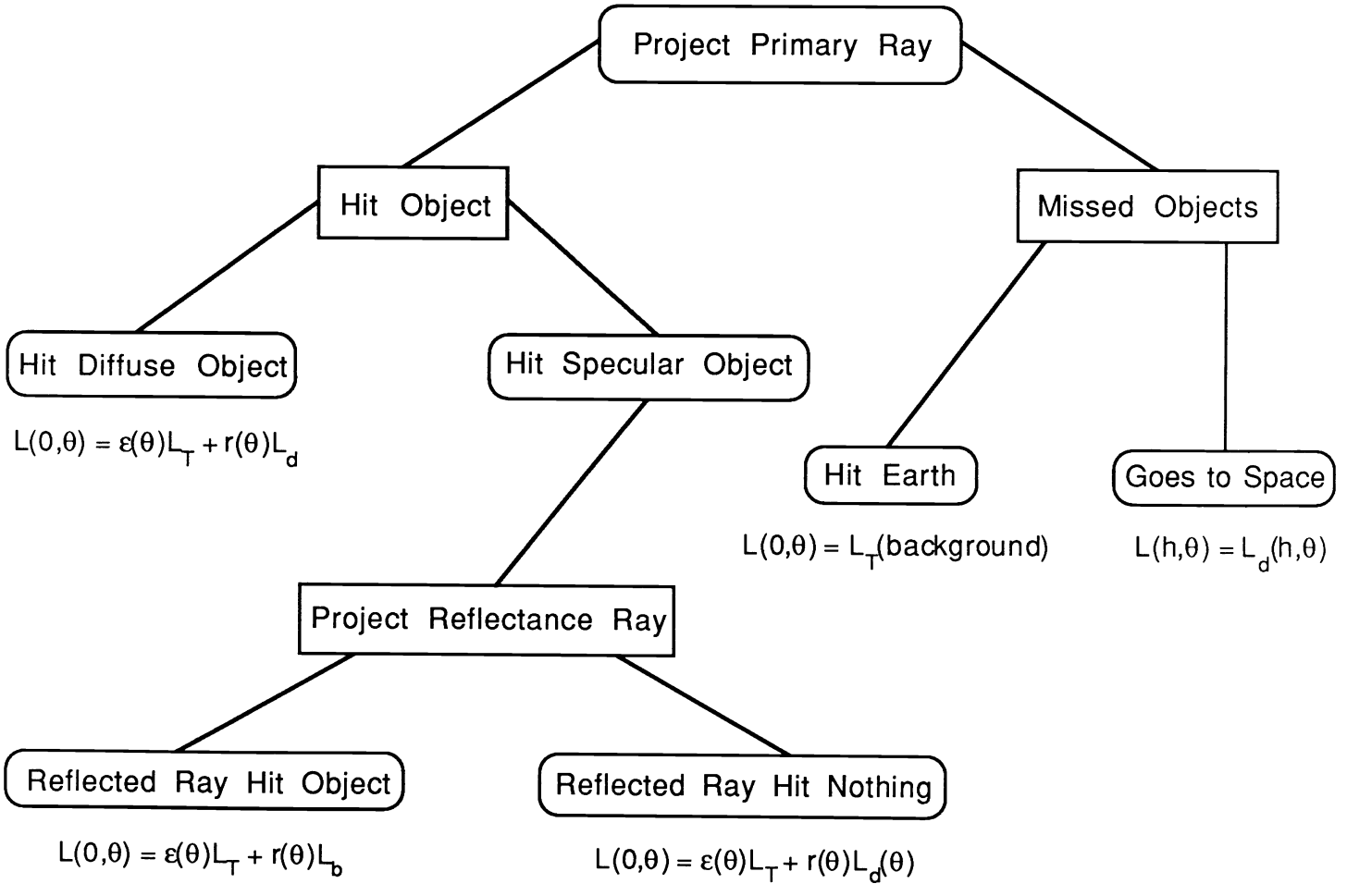

FIGURE 3 Description of ray projection performed for each pixel

In order to verify the accuracy of the simulator, it was decided to isolate and analyze two of the many parts that contribute to the model. The first part focuses on the geometric capabilities of the simulator and the second concentrates on the radiometric accuracy.

The geometric capabilities were demonstrated by depicting a complex scene consisting of a mobile missile transport vehicle on a road with a background composed of trees and grass. An image sequence was generated which varied the sensor location. Due to the complexity involved with physically creating a scene like the one described above, a simpler scene was created to test the radiometric fidelity. This experimental scene consisted of a wooden pyramid structure, a pool of water, and a warm background. The background was a tank of hot water which heated a sheet of black painted steel. All of these objects were placed on a concrete surface.

In order to get actual temperatures in the experimental scene, high-precision pre-calibrated thermistors were placed on the various objects. The real IR image was acquired with an Inframetrics 600L camera. Although the camera has a real-time temperature reporting capability, an in scene calibration was performed to achieve the desired accuracy. The calibration made use of a CI Systems SR 80 Extended Area Infrared Radiation Source (blackbody) settable from 0°C to 50°C. The IR camera imaged the blackbody at three different temperatures, and a calibration curve was constructed. This curve was later used to convert digital count values to apparent temperature. Once the IR image was acquired, local areas were averaged and converted to apparent temperature. These temperatures were compared against the SIG predictions.

In order to create the synthetic IR image of the experimental scene, the atmospheric conditions were entered into the model. This was done by using radiosonde data collected at a nearby airport on the evening the experiment was performed. The temperature data for the objects and the viewing parameters were entered into the model. The field-of-view for the IR camera was entered (20° horizontal, 15° vertical) along with the image size (500 by 408 pixels). The gain of the sensor was estimated from a knowledge of what the temperature range of the scene would be (approximately 5 DC / 1°K). The final radiometric image was then convolved with a 5 x 5 equal weight smoothing kernel to estimate typical degradations due to sensor sampling and optical effects.

RESULTS

Objects were created using a Intergraph (modified DEC VAX 11/785) computer running Intergraph-RandMicas (IRM) software. The user connected lines, planes, and surfaces to form the objects of interest. Finite element analysis techniques were used to represent the object as a number of triangular facets in cartesian coordinate space. Many objects were assembled to create a scene on a Silicon Graphics IRIS 3020. The user can rotate, translate, and scale each object. Once the user is satisfied with the scene, the facets are assigned material indices and temperatures. Material indices point to characteristics such as the angular emissivity data. The scene file was then input to the LWIR ray-tracing program on a DEC VAX 8350. The user defines where the camera is to be located along with image size, vertical and horizontal field-of-view, and sensor gain.

Two images are created, the radiance image and its' corresponding interaction map. The interaction map is used to help the user understand the radiometric effects at each pixel. For each pixel the material index of the first object a ray hits is recorded and shifted four bits to the left. If the material was specular, the reflection ray is cast out. The material index of the object hit by the reflection ray is placed in the lower four bits of one byte for the current pixel. If no objects were hit, then a zero DC is placed in these bits. This technique allows for 15 different materials (4 bits) giving 256 unique interactions (8 bits).

Figure 4 demonstrates one of the capabilities of the synthetic image generator. The scene depicts a mobile missile transport on a road with a background composed of trees and grass. The input specifications of the objects and radiometric parameters supplied to the SIG are given in Tables 1 and 2, respectively.

TABLE 1 Significant scene input specifications

Object	Material	# of Facets	Temperature*
Vehicle	Steel	500	290.30 K min/338.70 K max
	Glass	**	292.77 K
	Tires	**	300.00 K
Road	Asphalt	4	293.15 K
Trees	Conifer	72	289.15 K min/292.30 K max
Field	Grass	4	286.18 K

* Object temperatures based on data from a thermodynamic model with min and max based on statistical distribution of temperatures for that object.

** Included in 500 facets

TABLE 2 Input Parameters

Frame	Sensor Location			Rotations			Gain	Field of View	
#	X	Y	Z	x-axis	y-axis	z-axis		X	Y
		(km)			(degrees)		(DC/K)	(degrees)	
1	1.60	-3.00	0.70	78.3664	0.00	28.0725	2.0	1.0	1.0
2	0.80	-3.00	0.70	77.2948	0.00	14.9314	2.0	1.0	1.0
3	0.40	-3.00	0.70	76.9772	0.00	7.5946	2.0	1.0	1.0
4	0.00	-3.00	0.70	76.8660	0.00	0.0000	2.0	1.0	1.0
5	-0.40	-3.00	0.70	76.9772	0.00	-7.5946	2.0	1.0	1.0
6	-0.80	-3.00	0.70	77.2948	0.00	-14.9314	2.0	1.0	1.0
7	-1.60	-3.00	0.70	78.3664	0.00	-28.0725	2.0	1.0	1.0
8	-3.20	-3.00	0.70	80.9328	0.00	-46.8476	2.0	1.0	1.0

The images from the radiometric verification are shown below. Table 3 presents the

temperature data recorded during the experiment. Unfortunately, LOWTRAN 6 does not give accurate results for such a short path as used in this experiment (4.6m). In order for the simulation to work properly, experimental assumptions had to be made. The transmission, τ, was set equal to one, since visibility during the experiment was 15 miles. The upwelled path radiance was set to zero. This was justified because the experiment was over a path length of 4.6 m. The downwelled radiance term was calculated with the modified LOWTRAN.

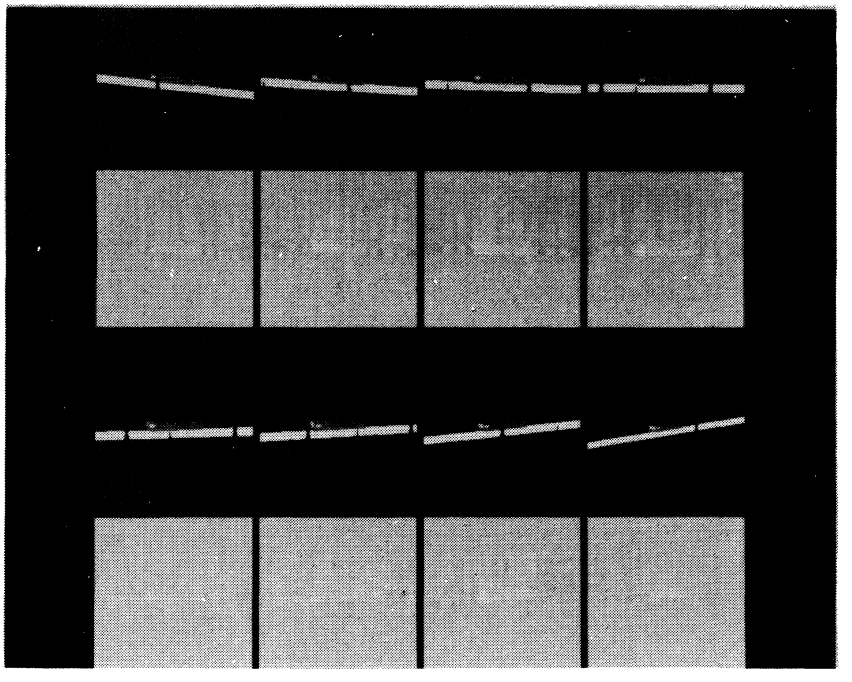

FIGURE 4 Simulated parallel "fly-by" sequence of a transport vehicle

TABLE 3 Radiometric Test (in ^{o}C)

	Assigned Temperature		Apparent Temperature of		
Location	Thermistor	Average	Real IR	$\varepsilon(60^{o})$	Synthetic IR
Top Pyramid	-0.68		-0.36	0.843	-3.97
Left Concrete	2.63	3.23	2.36	0.944	1.05
Right Concrete	3.84	3.23	2.71	0.944	1.05
Bottom Pyramid	0.97		2.17	0.843	1.20
Left Pool	13.77	13.35	9.62	0.925	10.04
Right Pool	12.93	13.35	12.88	0.925	15.31
Left Blackbody	38.15	34.99	37.02	0.747	32.34
Right Blackbody	31.83	34.99	35.57	0.747	31.29

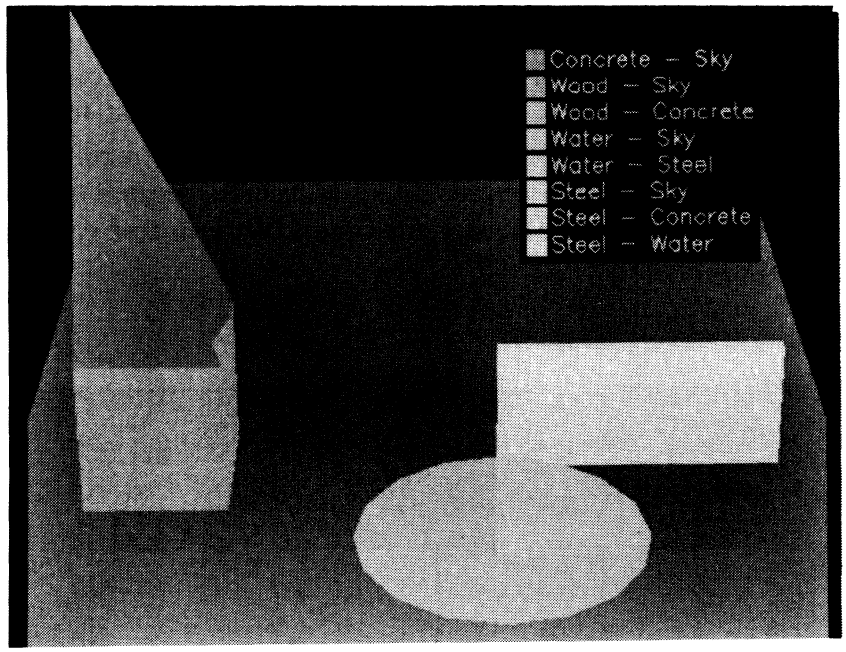

FIGURE 5 The interaction map from the LWIR ray-tracer. Notice the region of specular reflection from the pool of water (a specular material) and non-reflection from nearby concrete (a diffuse material).

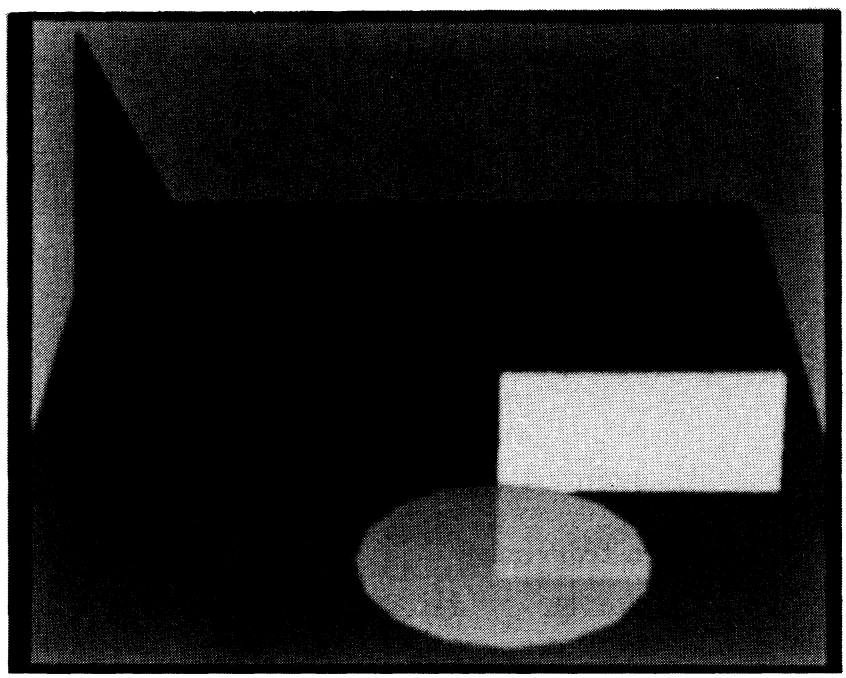

FIGURE 6 The radiance image produced to match the actual IR image FIGURE 7. The model predicts regions on the left side of the pyramid that show angular emissivity effects as well as the apparent difference in water temperature due to the background object.

FIGURE 7 The actual IR image acquired from an Inframetrics 600L camera.

CONCLUSIONS AND RECOMMENDATIONS

A visual comparison of the real and synthetic images shows striking similarities, indicating the geometric capabilities of the simulator. The SIG process being demonstrated also showed many of the IR anomalies that occur in actual IR imagery. One can see reflection from the background upon the pool and no reflection on the surrounding concrete. The gradual change in brightness along the right side of the pyramid is a result of proper modeling of angular emissivity effects.

Absolute temperature measurement is a very difficult task. Working outdoors increases the complexity involved in getting accurate results. However, conditions were controlled to keep many of the problems to a minimum, for example, the experiment was done several hours after sunset so that rapid changes in solar load could not affect target temperatures. Because the thermistors impact the surface being measured only temperature changes with time potentially insulated from the thermistors view. There was a slight breeze which may have affected the apparent temperatures of objects causing them to move towards the air temperature.

There are many individual reasons that contribute to temperature errors. An average error of 2.50°C with a standard deviation of 1.526°C was observed. These values were calculated by taking the absolute difference between apparent real IR and synthetic IR temperatures. The temperatures reported for the actual IR image were calculated using local area sampling and a calibration curve. The calibration and data sampling methods account for errors of approximately 1°C.

Shor (1990) demonstrated that errors as large as -1.5°C can be easily introduced by not including the shape factor. The IR camera was located on a wall 4.77 m above the experimental scene introduced a shape factor of approximately 0.75 which would have influenced all but the most specular surfaces (*e.g.* water). The shape factor is very important in some cases. For example, cold and/or low emissivity objects with warm backgrounds. If a fast enough computation became available, this parameter should be calculated and accounted for.

This simplified error analysis would suggest a biased error of approximate 1.5°C with a random error 1°C in good agreement with the observed experimental value of 2.5°C.

The SIG process presented here is only applicable to 8-14 μm imagery. In order to make the process applicable in the 3-5 μm band, solar flux must be accounted for. This modification is being included in on going efforts.

The description of scene objects is still one of the most difficult parts of the entire SIG process. A decision must made whether surfaces should be composed of solely triangular or if quadrangular facets should be allowed. Four vertex facets would reduce the amount of data used to represent an object. It is recommended that object-editing code be implemented to address each facet of an object and be capable of changing its material index and its temperature.

Most materials have some combination of a specular and diffuse component. Future work should evaluate errors generated from the use of just specular and diffuse reflectors instead of BRDF values. Of course the diffuse component would also have some shape factor associated with it.

REFERENCES

Clough, S.A., F.X. Kneizys, E.P. Shettle, and G.P. Anderson, "Atmospheric radiance transmittance: FASCOD2, "*Proc. of the Sixth Conference on Atmospheric Radiation*," Williamsburg, VA American Meterological Society, Boston, MA 141-144 (1986)

Kneizys, F.X., E.P. Shettle, W.O. Galley, J.H. Chetwynd, Jr., L.W. Abreu, J.E.A. Selby, S.A. Clough, and R.W. Fenn, "Atmospheric Transmittance/Radiance Computer Code LOWTRAN 6, Air Force Geophysics Laboratory, Optical Physics Division, 1983

Salvaggio, C., and Schott, J. R., "Laboratory Techniques for Assessment of Long Wave Infrared (LWIR) Radiometric Models for Synthetic Scene Generation," *Infrared Technology XIV*, Proc. SPIE (1989)

Schott, J.R., "Incorporation of Angular Emissivity Effects in Longwave Infrared Image

Models," *Infrared Technology XII*, Proc. SPIE 685 (1986)

Shor, E. H., "Three-Dimensional Longwave Infrared Synthetic Scene Simulation", M.S. Thesis, Rochester Institute of Technology, Center for Imaging Science (1990)

Sheffer, A.D., and J.M. Cathcart, "Computer generated IR imagery: a first principles modeling approach," Proc. SPIE 933 (1988)

Stets J, J. Conant, J. Gruninger, and B. Ryali, "Synthetic IR Scene Generation," *Infrared Systems and Components II*, H.M. Liaw, Editor, Proc. SPIE 890, pp. 130-146 (1988)